



Investigation of shear band evolution in amorphous alloys beneath a Vickers indentation

Hongwen Zhang ^a, Xiaoning Jing ^b, Ghatu Subhash ^{b,*}, Laszlo J. Kecskes ^c,
Robert J. Dowding ^c

^a Department of Materials Science and Engineering, Michigan Technological University, 1400 Townsend Drive, Houghton, MI 49931-1295, USA

^b Department of Mechanical Engineering-Engineering Mechanics, Michigan Technological University, 1400 Townsend Drive, Houghton, MI 49931-1295, USA

^c US Army Research Laboratory, Weapons and Materials Research Directorate, AMSRL-WM-MD, Aberdeen Proving Ground, MD 21005-5069, USA

Received 18 January 2005; received in revised form 25 March 2005; accepted 24 April 2005

Available online 13 June 2005

Abstract

Shear band formation has been known to be the dominant deformation mechanism at room temperature in bulk metallic glasses. However, many indentation studies have revealed only a few shear bands surrounding the indent on the top surface of the specimen. This small number of shear bands cannot account for the large plastic deformation beneath the indentations. Therefore, a bonded interface technique has been used to observe the slip-steps due to shear bands evolution. Vickers indentations were performed along the interface at increasing loads. At small indentation loads, the plastic deformation was primarily accommodated by semi-circular primary shear bands surrounding the indentation. At higher loads, secondary and tertiary shear bands were formed inside this plastic zone. A modified expanding cavity model was used to predict the plastic zone size characterized by the shear bands and to identify the stress components responsible for the evolution of various types of shear bands.

© 2005 Acta Materialia Inc. Published by Elsevier Ltd. All rights reserved.

Keywords: Shear band; Metallic glass; Vickers indentation; Hardness; Expanding cavity model

1. Introduction

Experimental evidence has shown that plastic deformation in amorphous alloys at room temperature is accommodated through the development of multiple shear bands [1–3]. Indentation test is still an attractive technique to study the deformation behavior of amorphous alloys for the following reasons. First, indentation tests, being not particular about sample size, are easy to perform. Second, the plastic deformation in the indented material is constrained locally around the indent, which facilitates the study of plastic flow of the amorphous alloys surrounding and underneath the

indentation. In addition, the direct comparison of instrumented indentation results with tensile and compressive responses has [4–6] further validated the indentation technique as an effective probe for understanding the physics of plastic deformation in amorphous alloys.

The popular instrumented nano-indentation technique has played a major role in elucidating the mechanisms of plastic flow in amorphous alloys, which include the relationship between hardness and yield strength, discrete plasticity and microstructural changes under indentation [7–10]. One of the interesting results is the discrete plasticity, which was identified as discrete pop-ins or flow serrations in the load–displacement curves. Wright et al. [6] speculated that the ‘pop-ins’ are the result of rapid strain accommodation by individual shear bands emitted discretely in sequence. Some researchers

* Corresponding author. Tel.: +1 906 487 3161; fax: +1 906 487 2822.
E-mail address: subhash@mtu.edu (G. Subhash).

have noted the correlation between the number of shear bands and the ‘pop-ins’ in load–displacement curves [4]. In reality, these so-called shear bands are the slip-steps left by the propagation of shear bands on the observed surface. In the present paper the ‘slip-steps’ of the shear bands are loosely referred as shear bands. However, detailed quantitative investigations of this correlation between the slip-steps and the pop-ins remain to be seen. Moreover, the number of circle-like slip-steps, surrounding either the Berkovich or Vickers indents on a top surface of the specimen [1,11], is far less than the number of serration flows (if each ‘pop-in’ corresponds to an individual shear band initiation [4,12]). These results may indicate that (1) most of the plastic deformation is accommodated by shear bands formed underneath the indents and only a few of these shear bands extend onto the indentation surface, (2) most of the shear bands locate inside these sharp indents and their slip-steps are later smoothed by the indenter surfaces during the loading process, and (3) these slip-steps are too small to be easily identified by the methods employed in these studies.

So far, only a small number of papers have reported the shear bands formation underneath indents [13,14]. Donovan [13] observed that the plastic zone beneath the indentation in $\text{Pd}_{40}\text{Ni}_{40}\text{P}_{20}$ metallic glass was mainly characterized by the radial incipient cracks and the curving Hartmann lines. In [14], several sets of slip-steps from shear bands were noticed by using a sharp indent under a load of 5 kg. The patterns close to the indenter are akin to the slip-line field patterns in plasticity theory. However, the large semi-circular slip-steps observed in experiments are beyond the predictive capability of the slip-line theory. This limitation may be due to the complex stress state beneath the indenter as opposed to the plane-strain condition presumed in the slip-line theory and the effects from the existence of a free surface.

For these reasons, the current study is devoted to a systematic investigation of microstructural changes of the amorphous alloy beneath a Vickers indentation subjected to a range of loads with varying durations. To explore the possible factors that affect shear band formation, the following considerations are incorporated into the experimental design and sample selection. First, to eliminate the effects of pre-existing nano-crystals (mainly precipitated during bulk metallic glass (BMG) preparation) on shear band formation, typical Zr-based BMGs with excellent glass forming abilities are chosen. $\text{Zr}_{57}\text{Nb}_5\text{Ni}_{12.6}\text{Cu}_{15.4}\text{Al}_{10}$ bulk amorphous alloy (Vit106), whose reduced glass transition temperature T_{rg} is 0.62, is utilized in the current investigation [11,15]. Second, to elucidate the shear bands (slip-steps) pattern beneath the indentation, Vickers indentations are performed along the bonded interface of a cylindrical specimen. The specimen is then split apart for observation of the shear bands beneath the indentations. Third, to clar-

ify the slip-step pattern evolution beneath the indenter, indentations are performed under gradually increasing loads and the orientation of the indenter is varied with respect to the interface.

Most recently, the authors came across a paper by Ramamurty et al. [16] where a similar study was conducted. However, there are several differences between the current work by the authors and [16]. First, in the current study, the evolution of shear bands in Vit106 is tracked from 10 to 1000 g, whereas in [16] the study was carried out at loads ranging between 500–5000 g on $\text{Pd}_{42}\text{Ni}_{40}\text{P}_{18}$ BMG. Second, the current study also identified an additional set of shear bands that was not presented in [16]. Third, the current work also tried to explain theoretically the stress components responsible for the evolution of various sets of shear bands in the plastic zone. A modified expanding cavity model is also proposed to estimate the plastic zone size at low loads (<500 g) and compared to other models available in the literature.

2. Experiments

Vitreloy 106 ($\text{Zr}_{57}\text{Nb}_5\text{Ni}_{12.6}\text{Cu}_{15.4}\text{Al}_{10}$) cylindrical ingots of 3 mm in diameter were prepared by arc melting and mould casting technique as described in [15]. The amorphous state of as-cast glassy alloy was verified by X-ray diffraction (XRD) and differential scanning calorimetry (DSC) as shown in Fig. 1. The bonded interface approach for observation of deformation patterns underneath indentation was employed as follows. A cylindrical sample was cut into two halves and the cut surfaces were polished to mirror finish. They were then

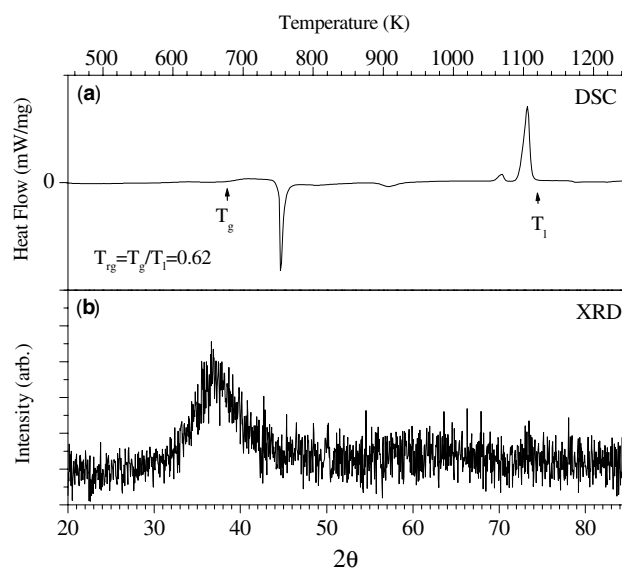


Fig. 1. Characterization of as-cast $\text{Zr}_{57}\text{Nb}_5\text{Ni}_{12.6}\text{Cu}_{15.4}\text{Al}_{10}$ bulk amorphous alloys by (a) DSC and (b) XRD.

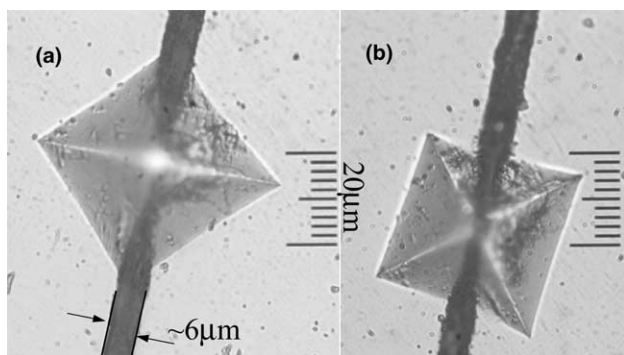


Fig. 2. Vickers indentation along the interface at different orientations: (a) interface parallel to the indenter diagonal and (b) interface at 45° to the indenter diagonal.

bonded together with rapid glue and clamped together tightly with specially designed clamp. The bonded specimen was then mounted into a mixture of epoxide resin and epoxide hardener. After solidification, the top surface of the sample was polished to mirror finish for indentation tests.

A Leco Vickers hardness tester was employed for quasi-static indentation tests. To monitor the load–time relationship during the indentation, a high frequency (~200 kHz) Kistler load cell with a load resolution of 0.1 N was placed under the sample. The total indentation cycle duration (consisting of loading, holding and unloading) was varied from 5 to 30 s. Normally, the maximum load was reached in much less than 1 s even for the 1000 g loading. Typical loading rates ranged from 10.7 to 26.9 N/s for the selected loads. The load was then held constant for a certain amount of time and then the sample was unloaded. Indentations were also performed along the interface with the diagonal of the indenter oriented either parallel to the interface or at 45° to the interface, as shown in Fig. 2.

To illustrate the effects of magnitude and duration of the indentation load on the hardness, indentations were also performed on the top surface away from the interface. At each selected load and time duration, at least five indentations were carried out to determine the average hardness. After the indentation tests, the samples were placed in an acetone bath for 24 h to remove the surrounding epoxide resin and the rapid glue along the interface. An optical microscope and a scanning electron microscope (SEM) were used to observe the shear band patterns surrounding and beneath the indentation.

3. Results

3.1. Indentation on flat surface

The hardness measured on the top surface away from the interface at selected loads and time durations is

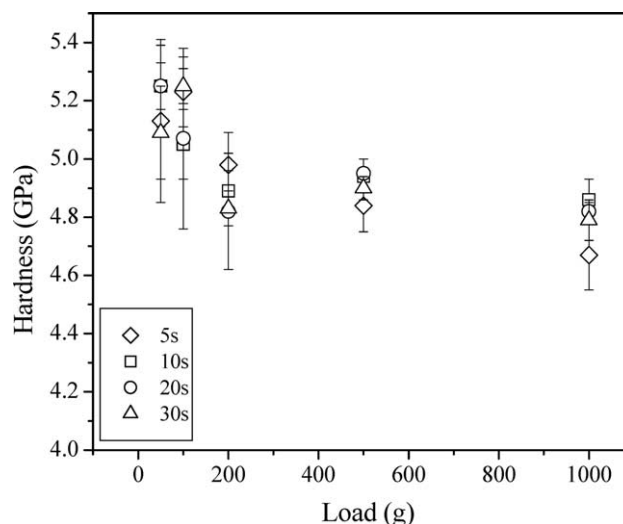


Fig. 3. Variation of Vickers hardness with load and loading time duration.

shown in Fig. 3. A slight decrease in hardness with increasing load is observed. However, at a given load, no evidence of variation in hardness value with increasing indentation duration was detected, which indicates that the plastic deformation under indentation was accomplished well within the time duration of less than 5 s (the smallest duration employed in the test). Typical indentation images on the top surface away from the interface are shown in Fig. 4. At a small load of 10 g, slip-steps of shear bands partially surrounding some edges of the indentation are clearly observed on the top surface in Fig. 4(a). Some partially developed slip-steps are also observed initiating from some corners of the indent and disappearing into the amorphous matrix. At a larger load of 500 g, curved slip-steps are occasionally observed only around one of the indent edges. In many cases, slip-steps can not be detected outside the indent. Note that in Fig. 4(b), some slip-steps seem to intersect with others. As will be explained later, these slip-steps may be associated with secondary or tertiary shear bands induced at large loads.

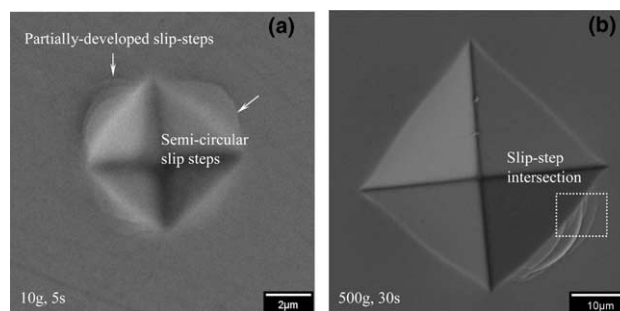


Fig. 4. Slip-step patterns resulting from shear bands propagation surrounding the Vickers indentation.

3.2. Indentation along the interface

Fig. 2 indicates a typical indentation on a specimen along the interface. It is seen that a fairly close bond is formed between the two halves where the width of the interface is measured to be around 6 μm and the size of the indentations (under a load of 200 g for the left image and 100 g for the right image) is observed to be significantly larger than the width of the interface. The confinement provided by the epoxide resin matrix surrounding the bonded sample holds the two halves together and does not allow separation even under an indentation load of 1000 g. Fig. 5 reveals the half indent at a load of 200 g and duration of 5 s on the top surface of one of the half samples after debonding, where the indenter diagonal is oriented parallel to the interface. A slightly out of plane protrusion ($\sim 3 \mu\text{m}$) at the center of the indent is observed, which implies a plastic flow normal to the bonded interface under the indentation. Recall that the width of interface is $\sim 6 \mu\text{m}$ (Fig. 2) and, hence, the $3 \mu\text{m}$ protrusion indicates that (1) the soft adhesive material in the interface does not provide rigid boundary condition but allows a plastic displacement of the material flow normal to the plane of the interface and (2) the constraint from the other half of the bonded specimen can only be effective when the displacement reaches half of the width of the interface.

Fig. 6 illustrates the evolution of deformation pattern on the vertical surfaces of the bonded sample indented at increasing loads and with the indenter diagonal oriented along the interface. In all the figures, a layered bulge at the tip of the indent is observed, which corresponds to the protrusion observed from the top surface in Figs. 2 and 5. As mentioned earlier, the layered bulges are caused mainly by the existence of ‘non-rigid surface’

along the interface and consequently, the material flows toward the interface. Notice from Fig. 6 that the depth of the bulge below the indentations increases from around 2.6 to 6.4 μm when the load increases from 10 to 1000 g. Immediately surrounding the bulge, several serrated semi-circular slip-steps due to shear bands are observed. Beyond the serrated slip-steps, numerous smooth semi-circular slip-steps of shear bands with spacing of 200–300 nm are seen when the load was increased above 50 g. These serrated and the smooth semi-circular slip-steps together are named ‘primary shear bands’ in order to distinguish them from other slip-steps due to shear bands that form at higher loads (>50 g). The number of the slip-steps from these primary shear bands increases dramatically with increasing load, but the spacing between them seems to remain constant. Interestingly, the slip-steps of these semi-circular primary shear bands seem to vanish as they approach the indentation surface (see Fig. 6(f)). The reason for this behavior will be explored in the next section. In all of the above indentations, it is noted that the lateral size of the region containing these primary shear bands does not extend beyond the diagonal size of the indent on the top surface. Therefore, typically no slip-steps of the shear bands are seen to extend beyond the diagonal of the indentation on the top surface as illustrated earlier in Fig. 4.

Above 100 g loading, two additional sets of the slip-step patterns occur inside the zone of primary shear bands, as shown in Figs. 6(c) and (d). They are named secondary and tertiary shear bands. The secondary shear bands either emanate radially (called secondary radial shear bands in Figs. 6(e) and (f)) from the tip of the indent (bulge area) or initiate along the top indentation surface (called secondary surface shear bands in Fig. 6(f)). The tertiary shear bands develop inside but close to the boundary of the primary shear bands region as shown in Fig. 6(e). They intersect with both primary and secondary radial shear bands but seldom approach the top surface of the indent.

Fig. 7 reveals the evolved shear bands pattern at a 1000 g load when one of the indenter boundaries is aligned parallel to the interface. Similar to the previous orientation, the slip-steps of the semi-circular primary shear bands as well as the radial and surface shear bands are seen. However, the slip-steps of the tertiary shear bands do not appear even at a load of 1000 g. Moreover, the central layered bulge is also significantly smaller as shown in Fig. 7(c), when compared with the previous micrographs shown in Fig. 6. This might be due to the fact that the sharp edges of the pyramid are away from the interface and therefore the intensity of deformation is less severe. Lack of tertiary shear band traces also further verifies that the intensity of deformation in this orientation is significantly less severe. Based on the above observations, it is reasonable to deduce that a

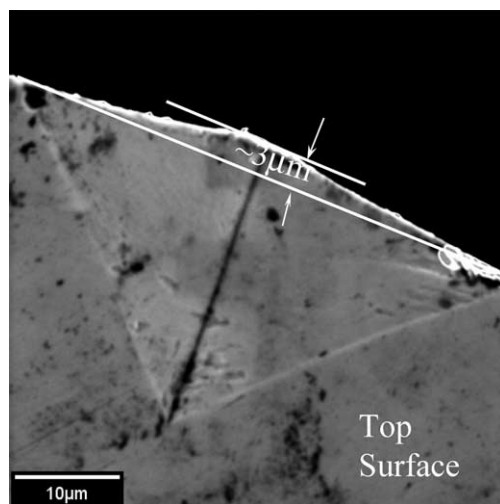


Fig. 5. Half indent revealing materials flow normal to the plane of interface.

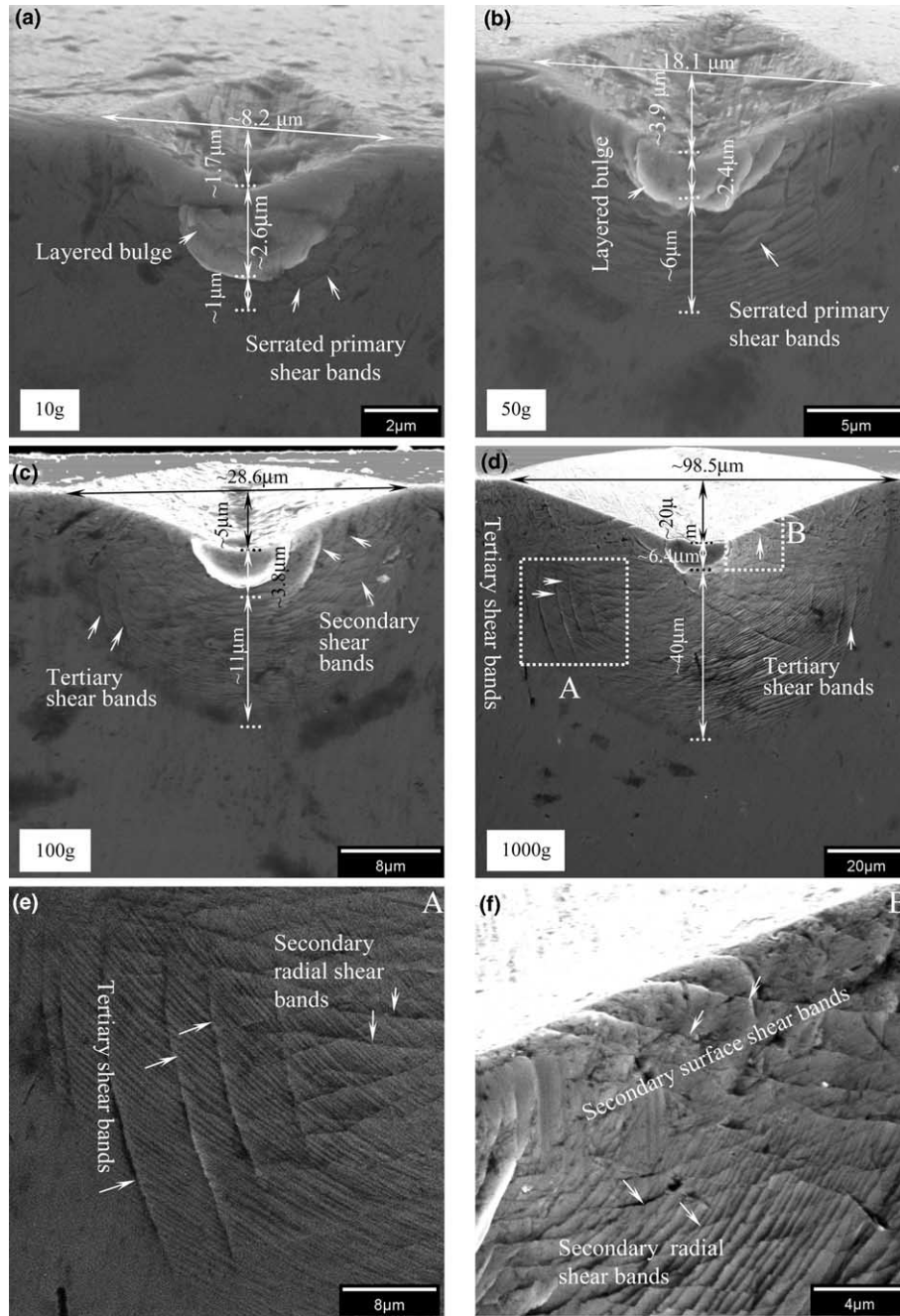


Fig. 6. Evolution of shear band patterns with load beneath the Vickers indentation when the indenter diagonal is aligned parallel to the interface.

hemispherical region of shear bands with different patterns is formed beneath the indentation.

4. Discussion

In many previous studies of Vickers indentations on amorphous alloys of different compositions [14,17,18], it was noted that a few slip-steps of shear bands were observed on the top surface surrounding the indents. Similarly, a few slip-steps of shear bands were also observed

surrounding the Berkovich indents [1,11]. This may indicate that whether the shear bands could propagate onto the top surface is not only dependent on the indenter shape but also on the load and the material microstructure (even for amorphous alloys, the local microstructural variation still exists, such as ordering in short range or middle range).

Beneath the Vickers indentation, the deformation patterns have been clearly illustrated in Figs. 6 and 7. However, the bonded interface does not provide continuous elastic constraint for the plastic flow, and hence

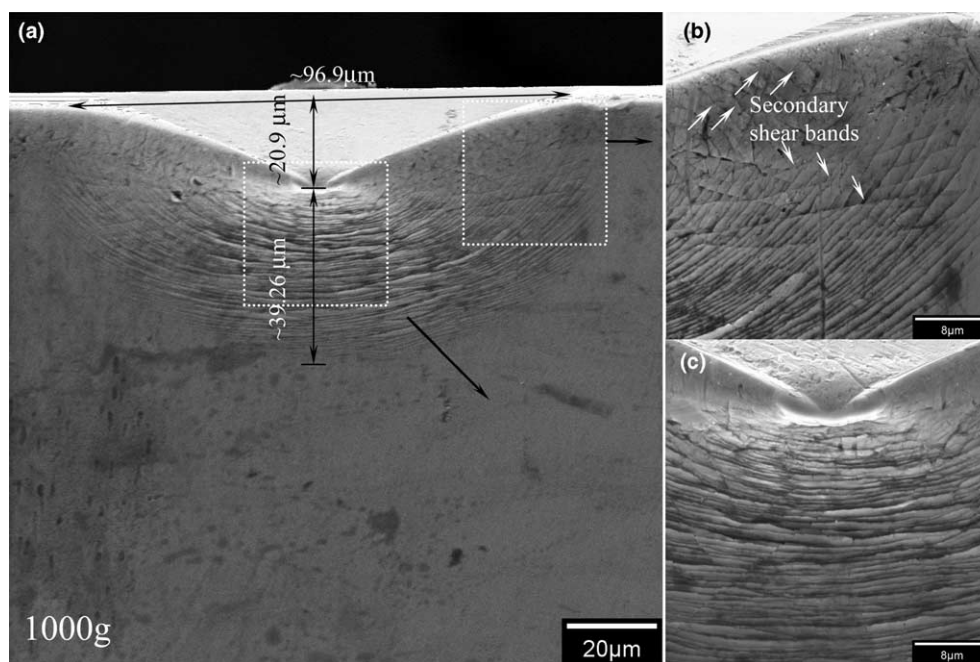


Fig. 7. Shear band pattern beneath a Vickers indentation when the indenter diagonal is aligned at 45° to the interface.

may produce a deformation zone which is different in size and shape from what would occur in a continuous bulk solid. Through extensive studies on various materials, Mulhearn [19] concluded that the relaxation of the constraint may affect the extent of the deformed zone and the strain gradient, but not the contours of the equivalent strain. Based on this premise, the current observation of shear band patterns could be considered to represent the deformation behavior beneath the indenter in the bulk solid. The von Mises equivalent stress contours, analyzed by a finite element model [20] beneath a pyramidal indenter for various materials, also have patterns similar to the semi-circular slip-steps of shear bands (primary shear bands) observed in the current study. However, the formations of both the secondary and the tertiary shear bands under elevated loads have not been predicted by the finite element model.

Slip-line field models and expanding cavity models are widely used to describe the plastic flow of the material beneath an indenter. From the current observations, few slip-steps of the shear bands reach the top surface, which indicates that the rigid plastic slip-line field models may not account for the deformation behavior of the amorphous material under consideration. Furthermore, the evolution of additional shear band patterns with increasing load also implies the limitation of the application of slip-line field model in present observations. In a simple stress state, such as uniaxial compression or pure bending, shear bands along certain angle relative to the loading axis are favorably formed to accommodate the local plastic strain [2,21]. The subsequent plastic deformation at increasing loads is generally accommodated

by branching of shear bands and cracking. However, the complex stress state of indentation tests causes various sets of shear bands at different orientations and locations beneath the indentation, instead of shear band branching and cracking. Similar to analytical models that try to explain formation of several indentation crack systems such as radial, median and lateral cracking in brittle solids [22], it seems reasonable to correlate the spatial location and orientation of these shear band patterns under different loads with the stress components in the indented specimen. Therefore, a modified expanding cavity model (ECM) based on the Drucker–Prager yield criterion [23] is employed to analyze the deformation behavior of the indented material beneath a Vickers indentation. To simplify the analysis of various stress components, the deformation is assumed to be axisymmetric. Although this is not fully in accordance with actual deformation under a Vickers indenter, the intent is to identify the relevant stress components that are responsible for the observed slip-step patterns of the shear bands.

Fig. 8 shows the schematic of the elastic–plastic region beneath an indentation described by the expanding cavity model. The Drucker–Prager yield function (e.g., see [23]) may be represented in spherical coordinates (r, θ, φ) by

$$\sigma_{\theta\theta} - \sigma_{rr} + \frac{1}{3}(\sigma_{rr} + 2\sigma_{\theta\theta}) \tan \alpha = \left(1 - \frac{1}{3} \tan \alpha\right) \sigma_y^c, \quad (1)$$

where α is the pressure sensitivity index which depends on the yield stress in uniaxial compression σ_y^c and the yield stress in uniaxial tension σ_y^t . Assuming that the

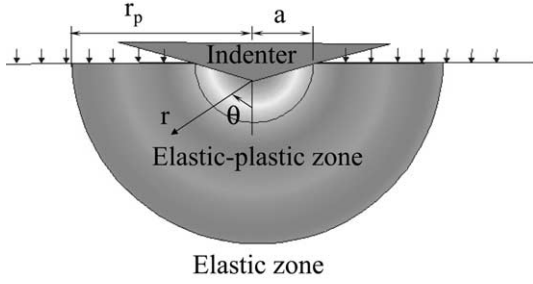


Fig. 8. Schematic of the modified expanding cavity model.

Drucker–Prager circular cone coincides with the outer apexes of the Coulomb–Mohr hexagon, α can be estimated as [24,25]

$$\alpha = \arctan \left[\frac{3(\sigma_y^c - \sigma_y^t)}{\sigma_y^c + 2\sigma_y^t} \right]. \quad (2)$$

The values of σ_y^c and σ_y^t in Eq. (2) for the sample material are listed in Table 1 [2]. Referring to Narasimhan [23], the stress components and the radial displacement in the elastic region ($r_p \leq r < \infty$) and the plastic region ($a \leq r < r_p$), where a is the equivalent indent contact radius and r_p is the radius of the plastic region (see Fig. 8), are given as follows:

In the elastic region ($r_p \leq r < \infty$),

$$\sigma_{rr} = -\frac{2}{3}\sigma_y^c \left(1 - \frac{1}{3}\tan\alpha\right) \left(\frac{r_p}{r}\right)^3, \quad (3a)$$

$$\sigma_{\theta\theta} = \frac{1}{3}\sigma_y^c \left(1 - \frac{1}{3}\tan\alpha\right) \left(\frac{r_p}{r}\right)^3, \quad (3b)$$

$$u_r = \frac{1}{3E}\sigma_y^c \left(1 - \frac{1}{3}\tan\alpha\right) (1 + \nu) \frac{r_p^3}{r^2}. \quad (3c)$$

In the plastic region ($a \leq r < r_p$),

$$\sigma_{rr} = -D\sigma_y^c \left(\frac{r_p}{r}\right)^{2q} + \frac{B}{q}\sigma_y^c, \quad (4a)$$

$$\sigma_{\theta\theta} = D(q-1)\sigma_y^c \left(\frac{r_p}{r}\right)^{2q} + \frac{B}{q}\sigma_y^c, \quad (4b)$$

$$u_r = \frac{\sigma_y^c}{E} \left[Mr_p \left(\frac{r_p}{r}\right)^{2q-1} - Lr_p \eta_\theta \left(\frac{r_p}{r}\right)^{s-1} + (1-2\nu) \frac{B}{q} r \right], \quad (4c)$$

where ν is the Poisson's ratio and B , q , D , L and M are defined as

Table 1
Properties of $\text{Zr}_{57}\text{Nb}_5\text{Ni}_{12.6}\text{Cu}_{15.4}\text{Al}_{10}$ bulk metallic glass [2]

Property	Value
Elastic modulus (GPa), E	86.7
Bulk modulus (GPa), K	118
Shear modulus (GPa), G	30.8
Yield strength (MPa)	
σ_y^c	1800
σ_y^t	1200
Density (g/cm^3), ρ	6.8
Poisson's ratio, ν	0.38

$$\begin{aligned} B &= \frac{1 - \frac{1}{3}\tan\alpha}{1 + \frac{2}{3}\tan\alpha}, \quad q = \frac{\tan\alpha}{1 + \frac{2}{3}\tan\alpha}, \\ D &= \frac{B}{q} + \frac{2}{3} \left(1 - \frac{1}{3}\tan\alpha\right), \\ L &= \frac{2(2q-3)(1-\nu)}{3-4q(\frac{1}{2} + \frac{1}{3}\tan\alpha)} Dq, \\ M &= L \left(\frac{1}{2} + \frac{1}{3}\tan\alpha\right) + (1-\nu)(q-1)D + \nu D. \end{aligned} \quad (5)$$

In the above analysis, the traction outside the indentation zone on the top surface of the specimen is not zero-valued, as shown in Fig. 8. This is one main limitation of the expanding cavity models when applied directly to the indentation problem. Chiang et al. [22] proposed to eliminate the non-zero normal stress field acting on the top surface by superposing inverse Bousinesq's point force elasticity solution [26]. They argued that the elastic superposition on the elastic–plastic stress fields is self-consistent due to the spherical symmetry of the plastic zone as well as the elastic–plastic boundary.

The stresses induced within the plastic zone by the surface forces result in the modification of the stress magnitudes in Eqs. (3) and (4) inside elastic and plastic zones. The stresses created by the surface forces have a general form [26]

$$\sigma_{mm} = \int_{V_{el}} G_{mm}\sigma_n^{el} dA + \int_{V_{pl}} G_{mm}\sigma_n^{pl} dA, \quad (6)$$

where σ_n^{el} and σ_n^{pl} are the normal stresses on the specimen surface within the elastic and the plastic zones, respectively. The subscript mm can be either rr , $\phi\phi$, zz or rz (the components in the cylindrical coordinate system (ρ, ϕ, z)) and G_{mm} are the point force functions given by [26]

$$\begin{aligned} G_{\rho\rho} &= \frac{1}{2\pi} \left[(1-2\nu) \left(\frac{1}{\rho^2} - \frac{z}{r\rho^2} \right) - \frac{3z\rho^2}{r^5} \right], \\ G_{\phi\phi} &= -\frac{1}{2\pi} (1-2\nu) \left(\frac{1}{\rho^2} - \frac{z}{r\rho^2} - \frac{z}{r^3} \right), \\ G_{zz} &= -\frac{1}{2\pi} \frac{3z^3}{r^5}, \\ G_{rz} &= -\frac{1}{2\pi} \frac{3\rho z^2}{r^5}. \end{aligned} \quad (7)$$

Transforming the above expressions into the spherical coordinates (r, θ, φ) and using $r^2 = \rho^2 + z^2$, one can obtain

$$\begin{aligned} G_{rr} &= G_{\rho\rho} \sin^2\theta + G_{zz} \cos^2\theta + 2G_{\rho z} \sin\theta \cos\theta, \\ G_{\theta\theta} &= G_{\rho\rho} \cos^2\theta + G_{zz} \sin^2\theta - 2G_{\rho z} \sin\theta \cos\theta, \\ G_{\varphi\varphi} &= G_{\phi\phi}. \end{aligned} \quad (8)$$

The formulas listed above will be used to numerically determine the stress components in the plastic zone, which will be used to explain the formation of various shear bands.

4.1. Geometry of deformation region beneath the Vickers indentation

Generally, shear bands initiate and propagate to accommodate the local plastic strain. The current observations reveal that the plastic deformation through the formation of various shear bands is mainly confined within a hemispherical region beneath the indenter. For some crystalline materials, the different sub-regions based on the characteristic plastic strain could be quantitatively distinguished [27,28]. It is hard to subdivide the plastic zone based on plastic strain in the current observations because of the lack of work hardening in amorphous alloys. However, the plastic zone characterized by various shear bands has been clearly detected, which is essential to determine the size of the deformation zone underneath the indentation.

Following Johnson's expanding cavity model [26,29], the radial displacement of the core boundary is assumed to accommodate the volume of material displaced by the indenter. Thus, the ratio of the plastic zone radius (r_p) to contact area radius (a) can be expressed as the following [26,29]:

$$\frac{r_p^3}{a^3} = \frac{E}{6(1-\nu) * \sigma_y^c} \cot \beta + \frac{2}{3} \frac{1-2\nu}{1-\nu}, \quad (9)$$

where E is the Young's modulus and $\beta = 70.3^\circ$, the equivalent half included angle of the indenter referred to [30]. Generally, the true contact area size can be extracted directly from the load–depth curve in an instrumented indentation test. To facilitate the analysis based on the expanding cavity model, an alternative way of estimating the size of contact area is employed. Based on the definition of the Meyer hardness $H = P_{\max}/A_{\text{cont}}$, where P_{\max} and A_{cont} are, respectively, the maximum load and the projected area of the indenter. The radius a of the projected area (see Fig. 8) can be obtained as $a = \sqrt{P_{\max}/(\pi H)}$.

Thus, the radius of the plastic zone can be estimated using Eq. (9) as:

$$r_p = \sqrt{\frac{P_{\max}}{\pi H}} \left\{ \frac{E}{6(1-\nu) * \sigma_y^c} \cot(\beta) + \frac{2}{3} \frac{1-2\nu}{1-\nu} \right\}^{\frac{1}{3}}. \quad (10)$$

The calculated size of the indentation as a function of load based on Eq. (10) is shown in Fig. 9 along with the experimentally measured radius of the plastic region from Fig. 6. In addition to the overall size of the plastic zone containing the shear bands, the bulge radius as well as the indentation depth from several other experiments are also indicated in Fig. 9 as a function of load. Because the hardness decreases with increasing load, an average Vickers hardness of 4.97 GPa (from Fig. 3) is employed to facilitate the calculation. A good agreement is seen at loads up to 500 g. At a load of 1000 g, the measured

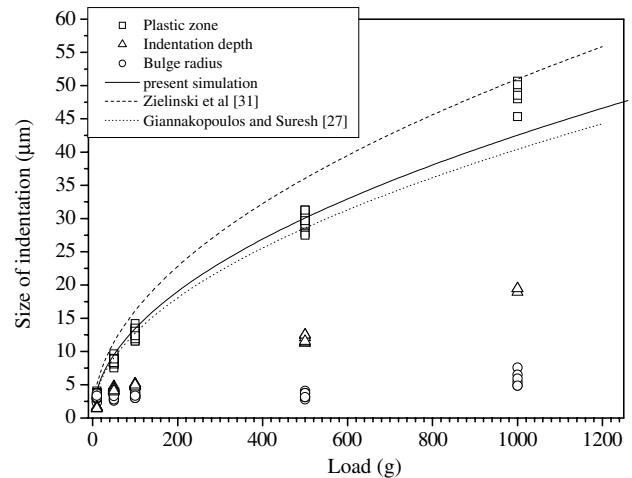


Fig. 9. Comparison of the experimentally measured plastic zone size with other models. The bulge radius and residual indentation depth measured from Fig. 6 are also included.

plastic region is slightly larger than that predicted by the current model (i.e., Eq. (10)). This deviation is probably due to the use of the average hardness value as opposite to the measured value under the load of 1000 g.

Giannakopoulos and Suresh [27] analyzed elastic–plastic properties of materials under instrumented indentation and proposed the following equation for the hemispherical plastic zone:

$$r_p = \sqrt{(0.3P_{\max})/\sigma_y^c}. \quad (11)$$

Based on indentation mechanics for single crystals, Zielinski et al. [31] proposed another equation for estimating plastic zone size as

$$r_p = \sqrt{(3P_{\max})/(2\pi\sigma_y^c)}. \quad (12)$$

The estimates from both Eqs. (11) and (12) are also plotted in Fig. 9. Clearly, the prediction by the current model falls in between those by the above two models, and the current model seems to provide a slightly better estimation than the above two models. Moreover, the predictions by Eq. (11) are better for loads below 500 g, and the predictions using Eq. (12) seem to be closer to the experimental results for loads beyond 500 g. A similar trend for plastic zone size with increasing load ($r_p \propto P_{\max}^{0.5}$) has also been reported recently [16].

4.2. Evaluation of stress field beneath the indentation

Although severe plastic deformation characterized by the distribution of various slip-steps of shear bands has been observed as shown in Figs. 6 and 7, it is still difficult to identify the origin of each set of shear bands. In general, under quasi-static uniaxial compression or pure bending, shear bands form at certain angle relative to

the loading axis. Branching of shear bands and even cracking have also been observed to occur at higher indentation loads [2,32]. In the current indentation tests, instead of shear band branching and cracking, additional sets of shear bands at different orientations and locations are developed inside the plastic zone to accommodate the intense plastic strain beneath the indentation. Therefore, it seems that different stress components may primarily be responsible for different sets of shear bands. Most recently, a unified failure criterion was proposed, by Zhang and Eckert [33], to account for the different fracture behavior of BMGs, metals, and brittle materials based on the ratio ($\alpha = \frac{\tau_0}{\sigma_0}$) between the critical shear fracture stress τ_0 and the critical normal fracture stress σ_0 . As summarized in their paper, normal tensile stress always plays some roles in the tensile fracture behavior. Zhang et al. [21] also summarizes the fracture angles for different BMGs under compressive loading, where the deviation of the fracture angles from 45° was referred to as the influence of normal stress in addition to shear stress on fracture. In the current situation, due to the non-uniform distribution of the stress beneath the indentation, it is reasonable to propose that some stress components may be responsible for the formation of certain set of shear bands in some regions.

The distribution of the three normal stress components (σ_{rr} , $\sigma_{\theta\theta}$, $\sigma_{\phi\phi}$) and the resulting maximum shear stress components ($\tau_1^{\text{cr}} = \frac{1}{2}(\sigma_{\theta\theta} - \sigma_{rr})$ and $\tau_2^{\text{cr}} = \frac{1}{2}(\sigma_{\phi\phi} - \sigma_{rr})$) underneath the indentation can be determined numerically through Eqs. (3)–(6) and (8). The resulting normalized stress components (σ_{rr}/p , τ_1^{cr}/p , and τ_2^{cr}/p , where p is the mean constant pressure) are plotted as a function of angle θ and radial distance r (see Fig. 8) in Fig. 10. In the following, it is assumed that the shear bands are formed when one of the stress components reaches a critical value at room temperature. Upon deciding the dominant stress component for each shear band pattern, both the absolute value of each of the stress components and the ratio between the two shear stress components and the radial stress, at certain loca-

tion beneath the indentation are considered to explain the formation of shear bands.

Inside the plastic zone, the modified ECM model reveals that the radial component σ_{rr} , normal to the spherical zone of the elastic–plastic boundary, is always negative, as shown in Fig. 10(a). The magnitude of σ_{rr} is the highest near the core area ($r = a$) and decreases gradually from the core to the elastic–plastic boundary ($r = r_p$). Close to the core, σ_{rr} first reach the yield stress when the load is large enough. Note that at a small indentation load of 10 g, only primary shear bands are observed (Fig. 6(a)) and the plastic zone containing these primary shear bands grows with increasing load. Thus, the formation of primary shear bands can be reasonably attributed to this radial stress component. Moreover, the ratio between the shear stress components and the radial stress close to the core area (~ 0.35) also indicates that radial stress may also contribute to the initiation of shear bands in that region. Furthermore, σ_{rr} decreases quickly in magnitude near the top surface ($\theta \rightarrow 90^\circ$) because of the relaxation of the surface forces. So this may illustrate why only a few primary shear bands can propagate to the top surface in our observation from Figs. 4 and 6(f).

Upon increasing the load, two maximum critical shear stress components $\tau_1^{\text{cr}} = \frac{1}{2}(\sigma_{\theta\theta} - \sigma_{rr})$ and $\tau_2^{\text{cr}} = \frac{1}{2}(\sigma_{\phi\phi} - \sigma_{rr})$ may reach shear yield stress τ_y (i.e., $\tau_y = 0.5\sigma_y$) as shown in Figs. 10(b) and (c). It is seen that these two stress components do not vary significantly in magnitude from $r = a$ to $r = r_p$ as compared to σ_{rr} in Fig. 10(a). However, a clear variation of the magnitude of these two stress components near the core area ($r = a$) is seen with θ , i.e., τ_2^{cr} decreases rapidly when $\theta > 60^\circ$, whereas τ_1^{cr} displays a peak value in the range $50^\circ < \theta < 70^\circ$. It is reasonable to assume that shear bands caused by these shear stress components may reveal different patterns as compared to the primary shear bands caused by the radial stress component. Thus, the secondary and the tertiary shear bands may possibly be caused by either or both of these two shear stress components.

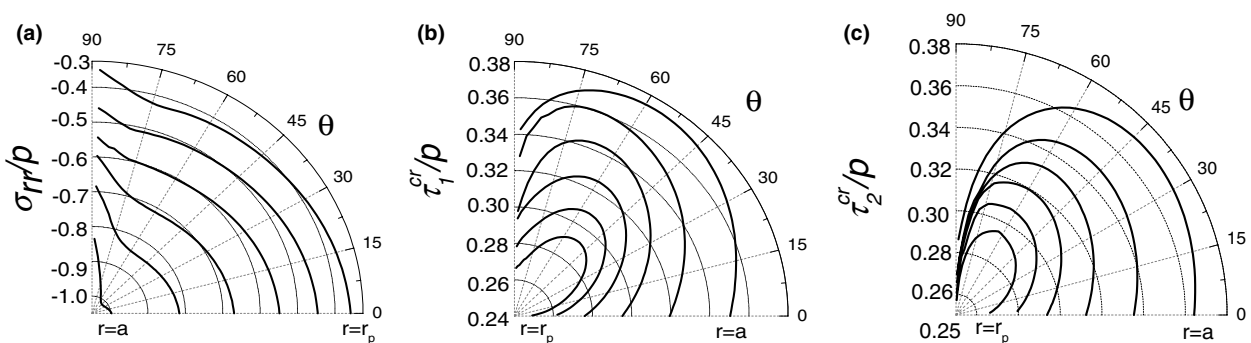


Fig. 10. Distribution of the normalized stress components beneath the indentation. Variation of (a) radial stress, (b) and (c) the maximum shear stresses as a function of the angle between the radius and the vertical direction defined in Fig. 8.

One of the characteristics of the secondary radial shear bands is that they extend from the core and cut across the entire elastic–plastic zone. Here, the minor variation in magnitude of certain shear stress component inside the plastic zone might account for the extension of the secondary radial shear bands. However, the assumption of parallel shear bands formation due to τ_1^{cr} and/or τ_2^{cr} leads to a controversy. Unlike the secondary radial shear bands, these secondary surface parallel shear bands (close to top surface) hardly extend across the whole plastic region. Recall that the confinement at the interface is non-rigid and hence the peripheral zone surrounding the indenter edge may not be accurately analyzed using the ECM. Gianakopoulos and Suresh [27] suggested a plastic cutting region close to the indentation edge, in which slip-line models, instead of expanding cavity models, are deemed to be more appropriate. Jana and co-workers [14,16,32] also found similar parallel secondary shear bands near the indentation edge, and suggested that the slip-line field analysis could be used to account for the shear band patterns.

Beyond a load of 100 g, three sets of slip-step patterns are observed in the current experiments as shown in Fig. 6(c). The slip-steps associated with the tertiary shear bands form mainly around the periphery of the elastic–plastic boundary between 50° and 70° (see Fig. 6(e)). These patterns may also be illustrated by the maximum critical shear stress component τ_1^{cr} (Fig. 10(b)), which reaches its peak value in the above range and thus could possibly explain their formation.

In Fig. 10(c), τ_2^{cr} decreases significantly when θ ranges from 65° to 90° . Consequently, τ_2^{cr} seems to more likely account for the secondary radial shear bands because of the smaller value close to the top surface and a larger value at θ below 70° . But few secondary radial shear bands can be observed right beneath the indenter, because the dense primary shear bands in that range relax most of the local severe plastic strain. Thus the above approach based on the stress components seems to logically explain the formation of various sets of shear bands.

Although the ECM was used here to explain the stress components responsible for each set of shear bands, the model has many limitations. First, from this model, the authors can only obtain the distribution of different stress components underneath the indentation which may dominate in the formation of a specific set of shear bands but it is not possible to determine the slip plane of the shear bands caused by each of the stress components. Recall that the primary shear bands continue to form as the load continues to increase. Formation of each shear band alters the stress state beneath the indentation. This modification of stress field continues with the formation of new sets of secondary and tertiary shear bands. The current modified ECM model, based on continuum elastic–plastic theory, does not directly

account for such discrete stress release effects when shear bands are formed. Moreover, the sharp-edge effects associated with a Vickers indenter are also not taken into account. From Fig. 7, it appears that the absence of tertiary shear bands could be attributed to the less severe stress state when the indenter diagonal is aligned 45° relative to the interface than that observed when the indenter diagonal is aligned parallel to the interface, as shown in Fig. 6. This model fails to capture such orientation effect due to the axisymmetric assumption. Also the evolution of shear bands is proposed purely based on the variation in the magnitude of stress components within the plastic zone without any reference to a criterion for shear band initiation. Despite these limitations, the model provides a fairly good estimation of the plastic zone size (Fig. 9) and also furnishes a simple explanation for exploring the formation of various sets of shear bands based on the evolving stress state beneath the indentation.

5. Conclusion

A bonded interface technique is successfully used to investigate the formation of various sets of shear bands beneath a Vickers indentation in BMGs. At small indentation load, only semi-circular primary shear bands surrounding the indent are observed. With increasing load secondary and tertiary shear bands are developed inside this plastic region. A modified ECM was used to predict the size of the plastic zone as a function of load. This model provides a good estimate of the plastic zone size compared to other models available in the literature. Based on the stress distribution inside the hemispherical plastic zone, the radial stress component has been identified as being responsible for primary semi-circular shear bands formation, and shear stress components for secondary and tertiary shear band formation.

Acknowledgments

The work reported here was funded by the Army Research Laboratory, Aberdeen Proving Ground, MD 21005-5069, and a grant from the US NSF (Grant # CMS-0324461) with Dr. Ken Chong as the program manager.

References

- [1] Vaidyanathan R, Dao M, Ravichandran G, Suresh S. *Acta Mater* 2001;49:3781.
- [2] Conner RD, Li Y, Nix WD, Johnson WL. *Acta Mater* 2004;52:2429.
- [3] Xing L-Q, Li Y, Ramesh KT, Li J, Hufnagel TC. *Phys Rev B* 2001;64:180201.

- [4] Golovin YI, Ivogin VI, Khonik VA, Kitagawa K, Tyurin AI. *Scr Mater* 2001;45:947.
- [5] Schuh CA, Argon AS, Nieh TG, Wadsworth J. *Philos Mag A* 2003;83:2585.
- [6] Wright WJ, Saha R, Nix WD. *Mater Trans* 2001;42:642.
- [7] Schuh CA, Nieh TG. *J Mater Res* 2004;19:46.
- [8] Schuh CA, Nieh TG. *Acta Mater* 2003;51:87.
- [9] Bei H, Lu ZP, George EP. *Phys Rev Lett* 2004;93:125504.
- [10] Jiang WH, Pinkerton FE, Atzmon M. *J Appl Phys* 2003;93:9287.
- [11] Zhang HW, Subhash G, Kecskes LJ, Dowding RJ. *Scr Mater* 2003;49:447.
- [12] Wang JG, Choi BW, Nieh TG, Liu CT. *J Mater Res* 2000;15:798.
- [13] Donovan PE. *J Mater Sci* 1989;24:523.
- [14] Jana S, Ramamurty U, Chattopadhyay K, Kawamura Y. *Mater Sci Eng A* 2004;375–377:1191.
- [15] Gu X, Xing LQ, Hufnagel TC. *J Non-Cryst Solids* 2002;311:77.
- [16] Ramamurty U, Jana S, Kawamura Y, Chattopadhyay K. *Acta Mater* 2005;53:705.
- [17] Inoue A, Shen BL, Koshida H, Kato H, Yavari AR. *Acta Mater* 2004;52:1631.
- [18] Hajlaoui K, Benameur T, Vaughan G, Yavari AR. *Scr Mater* 2004;51:843.
- [19] Mulhern TO. *J Mech Phys Solids* 1959;7:85.
- [20] Giannakopoulos AE, Larsson P-L, Vestergaard R. *Int J Solids Struct* 1994;31:2679.
- [21] Zhang ZF, He G, Eckert J, Schultz L. *Phys Rev Lett* 2004;91:045505.
- [22] Chiang SS, Marshall DB, Evans AG. *J Appl Phys* 1982;53:298.
- [23] Narasimhan R. *Mech Mater* 2004;36:633.
- [24] Khan AS, Huang SJ. *Continuum theory of plasticity*. New York (NY): Wiley; 1995.
- [25] Chen WF, Han DJ. *Plasticity for structural engineers*. Berlin: Springer; 1988.
- [26] Johnson KL. *Contact mechanics*. Cambridge: Cambridge University Press; 1985.
- [27] Giannakopoulos AE, Suresh S. *Scr Mater* 1999;40:1191.
- [28] Chaudhri MM. *Acta Mater* 1998;46:3047.
- [29] Johnson KL. *J Mech Phys Solids* 1970;18:115.
- [30] Li M, Chen WM, Liang NG, Wang LD. *J Mater Res* 2004;19:73.
- [31] Zielinski W, Huang H, Gerberich WW. *J Mater Res* 1993;8:1300.
- [32] Jana S, Bhowmick R, Kawamura Y, Chattopadhyay K, Ramamurty U. *Intermetallics* 2004;12:1097.
- [33] Zhang ZF, Eckert J. *Phys Rev Lett* 2005;94:094301.